

Probing electrical double layer via triboelectric charge transfer

Received: 12 June 2025

Accepted: 19 November 2025

Cite this article as: Wei, Y., Li, X., Gu, Y. *et al.* Probing electrical double layer via triboelectric charge transfer. *Nat Commun* (2025). <https://doi.org/10.1038/s41467-025-67094-9>

Yu Wei, Xiang Li, Yu Gu, Lian Ding, Xiang Gao, Zhongqiang Zhang, Carita Kvarnström, Johan Bobacka, Ari Ivaska, Zhong-Qun Tian, Zhong Lin Wang & Di Wei

We are providing an unedited version of this manuscript to give early access to its findings. Before final publication, the manuscript will undergo further editing. Please note there may be errors present which affect the content, and all legal disclaimers apply.

If this paper is publishing under a Transparent Peer Review model then Peer Review reports will publish with the final article.

1 Probing Electrical Double Layer via Triboelectric Charge 2 Transfer

3 Yu Wei ^{1, 2, #}, Xiang Li ^{1, 2, #}, Yu Gu ^{3, #}, Lian Ding ³, Xiang Gao ⁴, Zhongqiang Zhang ⁴, Carita
4 Kvarnström ⁵, Johan Bobacka ⁶, Ari Ivaska ⁶, Zhong-Qun Tian^{3, *}, Zhong Lin Wang ^{1, *}, and Di
5 Wei ^{1, 7, *}

6 ¹ Beijing Institute of Nanoenergy and Nanosystems, Chinese Academy of Sciences, Beijing, P. R. China

7 ² School of Nanoscience and Engineering, University of Chinese Academy of Sciences, Beijing, P. R. China

8 ³ School of Electronic Science and Engineering, State Key Laboratory of Physical Chemistry of Solid Surfaces, College of Chemistry and Chemical
9 Engineering, IKKEM, Xiamen University, Xiamen, China

10 ⁴ School of Mechanical Engineering, Jiangsu University, Zhenjiang 212013, P. R. China

11 ⁵ Department of Chemistry, University of Turku, Henrikinkatu 2, 20500 Turku, Finland

12 ⁶ Laboratory of Molecular Science and Engineering, Johan Gadolin Process Chemistry Centre, Faculty of Science and Engineering, Åbo Akademi University,
13 Henriksgatan 2, FI-20500, Turku, (Åbo), Finland

14 ⁷ Centre for Photonic Devices and Sensors, University of Cambridge, 9 JJ Thomson Avenue, Cambridge, UK

15 [#] These authors contributed equally to this work

16 ^{*} Corresponding authors' e-mail addresses: zqtian@xmu.edu.cn, zlwang@binn.cas.cn, weidi@binn.cas.cn.

17

18 Abstract

19 The nanoscale electrical double layer (EDL) governs macroscopic phenomena such as ion adsorption
20 and reaction kinetics, serving as a fundamental determinant in diverse applications ranging from sensing,
21 and catalysis, to energy storage. While classical EDL models primarily describe conductive interfaces,
22 most naturally occurring EDLs form at non-conductive surfaces in liquid environment, where
23 characterization remains fundamentally challenging due to the constraints of conventional techniques.
24 Here, we present a triboelectric nanogenerator (TENG)-based triboelectric charge transfer probe that
25 utilizes the intrinsic solid-liquid contact electrification (CE) process to operando monitor the formation
26 and evolution of the EDL at non-conductive interfaces. This bias-free and electrode-independent
27 approach enables direct probing of interfacial charge dynamics fundamentally inaccessible to

28 conventional electrochemical approaches constrained by conductive substrate dependencies and external
29 potential requirements. This method also reveals distinct EDL behaviors, particularly in electrolytes with
30 asymmetric ion sizes at concentrations exceeding 10^{-1} M and at non-conductive interfaces. Its
31 fundamental mechanism and measurement precision were rigorously validated via atomic force
32 microscopy, Kelvin probe force microscopy, surface-enhanced Raman spectroscopy, and molecular
33 dynamics simulations, establishing a robust analytical platform and theoretical basis for EDL studies.
34 This work introduces a CE-based methodology for direct triboelectric charge characterization on
35 dielectric surfaces, overcoming conventional conductive substrate limitations. By integrating classical
36 EDL theory with triboelectric frameworks, we establish models resolving interfacial charge dynamics
37 across diverse solid-liquid interfaces, including high ionic strength regimes. It confirms material-agnostic
38 applicability. This paradigm simultaneously advances fundamental EDL mechanisms and enables
39 programmable charge manipulation for next-generation iontronic power, sensing, and neuromorphic
40 devices.

41

42 Introduction

43 The electrical double layer (EDL)^[1], formed at solid-liquid or liquid-liquid interfaces, etc., is fundamental
44 to energy storage^[2, 3], catalysis^[4], and colloidal stability^[5], critically affecting reaction kinetics^[6],
45 corrosion resistance^[7], sensor performance^[8], and device efficiency across disciplines. The concept was
46 first introduced by Hermann von Helmholtz in the 19th century^[9], who proposed that charges on a metal
47 surface are compensated by a compact layer of counterions. While foundational, this model is overly
48 idealized, neglecting ion mobility and solvent effects, and cannot accurately describe charge distribution
49 or potential variation at real interfaces. In the early 20th century, Gouy and Chapman independently
50 extended this view by introducing a diffuse ion layer governed by electrostatic forces and thermal
51 fluctuations, leading to the Gouy-Chapman model^[10]. This framework captures the exponential decay of
52 ion concentration with distance from the surface but treats ions as point charges, ignoring their finite size,
53 hydration shells, and specific adsorption. To overcome these limitations, Stern proposed the Gouy-
54 Chapman-Stern (GCS) model in 1924^[11], combining Helmholtz's compact layer and Gouy-Chapman's
55 diffuse layer. The GCS model partitions the interface into the inner Helmholtz plane (IHP), comprising
56 the charged electrode surface and specifically adsorbed ions, and the outer Helmholtz plane (OHP),
57 consisting of solvated ions, together forming the Stern layer, beyond which the diffuse layer extends into
58 the bulk. At low electrolyte concentrations, this model effectively captures ion distribution and dynamics
59 near charged interfaces. While classical EDL theory has traditionally been applied to conductive
60 interfaces, recent studies demonstrate that dielectric materials can also sustain EDL formation^[5, 12, 13].
61 Nevertheless, conventional models are inadequate for non-conductive solid interfaces, owing to
62 experimental limitations in directly probing EDL structure. Their applicability further diminishes at high
63 ionic strengths ($>10^{-1}$ M), where interfacial ion correlations^[14], steric exclusion effects^[15], and specific
64 adsorption energetics dominate interfacial reorganization. Moreover, the model neglects solvent
65 structuring, non-local dielectric responses, and interfacial dynamics such as polarization and specific ion
66 adsorption. These limitations become especially evident in systems exhibiting charge inversion, a
67 nontrivial phenomenon in which accumulated counterions exceed what is required to neutralize the
68 surface charge. Charge inversion arises from a complex interplay of ion asymmetry^[16], hydrophilicity^[17],
69 hydrophobicity^[18, 19], and surface charge density^[20, 21], especially with asymmetric ions (in size, valency,

70 or polarizability) enhancing correlations that promote overcompensation. Despite growing experimental
71 and simulation-based evidence, the molecular-scale mechanisms underlying such behaviors remain
72 incompletely understood. These challenges underscore the need for advanced theoretical models and
73 interface-sensitive measurement techniques capable of capturing the full complexity of EDL structures
74 at non-conductive surfaces and under high ionic strength.

75 The EDL, a fundamental interfacial structure governing charge transfer and electrochemical
76 dynamics, has been explored through a wide range of experimental techniques. For conductive
77 interfaces^[22, 23], methods such as electrochemical impedance spectroscopy (EIS), cyclic voltammetry,
78 and scanning electrochemical microscopy (SECM) offer sensitivity to potential-dependent ion
79 redistribution. However, they are limited by electrode polarization, and substrate requirements,
80 particularly at high electrolyte concentrations where interfacial reactions may occur. A range of advanced
81 techniques has also been developed to investigate the structural characteristics of EDL, each with distinct
82 advantages and limitations. Optical spectroscopic methods, such as in situ Raman spectroscopy^[24],
83 surface-enhanced Raman spectroscopy (SERS)^[25, 26], and infrared spectroscopy^[27], are widely used for
84 their molecular sensitivity. In situ Raman spectroscopy enables non-destructive analysis but suffers from
85 low sensitivity and fluorescence interference. SERS significantly enhances signal intensity, allowing the
86 detection of trace species, yet it relies on carefully engineered plasmonic substrates, involves high
87 fabrication costs, and presents challenges in spectral interpretation. Infrared spectroscopy offers
88 molecular fingerprinting capabilities but is hindered by strong water absorption and poor suitability for
89 real-time studies. Atomic force microscopy (AFM)-based techniques^[28], such as Kelvin probe force
90 microscopy (KPFM), allow direct probing of interfacial potential and dielectric properties under realistic
91 electrolyte conditions with nanoscale resolution. However, KPFM measurements are strongly influenced
92 by tip geometry, long-range electrostatic coupling, and the dielectric environment. While KPFM
93 measures surface potential/work function on insulators, charge accumulation and slower dissipation on
94 insulating surfaces cause lower signal-to-noise ratios and susceptibility to charge injection interference,
95 posing greater challenges than conductor/semiconductor measurements. Additionally, it only provides
96 potential information rather than direct charge transfer measurements and extracting surface charge
97 requires complex modeling and calibration. Quartz crystal microbalance (QCM) offers high sensitivity

98 to mass changes and is valuable for tracking EDL dynamics, but it typically requires conductive or
99 specially coated substrates and stringent control over experimental conditions^[29]. X-ray-based methods
100 provide atomically resolved information on the arrangement of ions and molecules at interfaces, making
101 them powerful tools for the structural analysis of EDL^[30]. Nonetheless, they struggle with detecting liquid,
102 especially in aqueous or complex environments, and their reliance on specialized, expensive equipment
103 further limits accessibility. Theoretical computational methods offer atomic-level insights into EDL
104 formation and ion distribution but often fall short of capturing the complexity of real interfacial systems,
105 resulting in discrepancies with experimental observations. Therefore, despite the wide array of available
106 techniques, a reliable and straightforward testing method capable of probing EDL structures at non-
107 conductive interfaces, particularly under high-concentration electrolyte conditions, remains elusive.
108 Conventional techniques are often ineffective at probing these interfaces, necessitating alternative
109 approaches.

110 Contact electrification (CE), one of the oldest documented physical phenomena^[31], is traditionally
111 regarded as a surface charge transfer between dissimilar materials upon contact and separation. However,
112 it has recently undergone a scientific resurgence. Far from being fully resolved, CE has re-emerged as a
113 rich platform for exploring fundamental interfacial processes at the molecular scale. Recent findings
114 demonstrate that contact-induced charge transfer can also occur between identical insulators, giving rise
115 to spontaneous long-range electrostatic ordering^[32]. Investigations at oil-water interfaces reveal that the
116 electric fields originate directly from the contact between the water and oil interface^[33]. Collectively,
117 these advances reposition charge transfer based on CE as a contemporary frontier in interfacial science,
118 bridging solid-solid and liquid-liquid interfaces while offering mechanistic insights into the origins of
119 interfacial charge, dielectric asymmetry, and electrostatic ordering in complex environments. Notably,
120 charge transfer based on CE is particularly prominent at solid-liquid interfaces, where dielectric solids
121 interact with liquids to produce intricate interfacial phenomena^[34-37]. Solid-liquid triboelectric
122 nanogenerators (TENGs) based on CE have also emerged as highly sensitive probes for detecting charge
123 transfer between droplets and dielectric surfaces^[36-39], and for capturing rapid interfacial dynamics, such
124 as those observed in the Leidenfrost effect^[40], thereby enabling real-time insights into charge evolution
125 at dynamic interfaces. At these interfaces, the solid surface engages in intricate interactions with ions and

126 molecules in the liquid phase, initiating processes including electron transfer, ion exchange, and EDL
127 formation. Recent studies have proposed a “two-step” EDL model^[12] extending the GCS framework to
128 dielectric solid-liquid interfaces. First, contact between a dielectric solid and water induces electronic
129 polarization through electron cloud overlap and hydrogen-bonding interactions, while surface groups
130 undergo partial ionization to generate localized fixed charges. This defines the IHP, comprising the
131 charged solid surface and specifically adsorbed ions. In the second stage, ions in the liquid redistribute
132 to compensate these charges, forming the OHP. The IHP and OHP together form the Stern layer, a
133 compact region where most of the interfacial potential drop occurs. Beyond it, the diffuse layer exhibits
134 a gradual transition to bulk concentration and remains more sensitive to external conditions. The EDL as
135 a whole dictates the fundamental properties of the solid-liquid interface. Unlike conductor-based models,
136 where mobile surface electrons sustain the EDL under applied voltage, dielectric systems rely on an
137 electrostatically asymmetric and partially immobile polarization layer. The two-step model has since
138 been widely applied across diverse contexts and provides a foundation for triboiontronics, enabling
139 dynamic reconfiguration of dielectric-liquid EDLs via triboelectric field modulation and precise control
140 of ion transport kinetics^[41-43]. This strategy unlocks new possibilities for high-efficiency energy
141 scavenging, neuromorphic ionic logic, and self-powered information systems. Despite significant
142 progress, EDL behavior in high-concentration and asymmetric electrolyte systems remains largely
143 unexplored, representing a critical gap in current understanding. Moreover, the lack of effective probing
144 methods for EDLs on non-conductive surfaces has hindered deeper insights into interfacial charge
145 dynamics. Addressing these challenges is of fundamental importance for deciphering the diverse charge
146 signatures observed across electrolytes during CE and for unveiling the dynamic evolution of EDLs at
147 solid-liquid interfaces. Utilizing triboelectric charge measurement with a TENG, offering direct access
148 to CE-induced charge, provides a promising platform for the investigation of EDL formation on dielectric
149 surfaces. Such approaches hold immense potential for advancing interfacial iontronic charge regulation,
150 with far-reaching implications in various applications.

151 In this study, a disruptive alternative is presented that harnesses TENG as a straightforward
152 operando probe to elucidate the formation and evolution of EDLs across a wide range of electrolyte
153 concentrations. Unlike conventional methods requiring conductive interfaces and external bias, this

154 TENG-based triboelectric charge transfer probe enables bias-free, straightforward testing of interfacial
155 charge density on non-conductive surfaces, effectively circumventing Faradaic interference and
156 preserving the native EDL structure. It reveals the diverse static EDL architectures formed by various
157 electrolytes, including under high ionic strength conditions and at the non-conductive interfaces. It
158 confirms material-agnostic applicability. KPFM, SERS, and molecular dynamics (MD) simulations are
159 integrated as validation tools to confirm the accuracy of the triboelectric charge probe and to provide
160 complementary spectroscopic and atomistic insights. Collectively, these advances establish TENG-based
161 triboelectric charge transfer probing as a substrate-agnostic platform for interfacial iontronic
162 investigations. Its non-perturbative nature enables zero-bias interrogation of native EDL structures, even
163 in dynamic systems like high-flow-rate electrolytes while revealing fundamental insights into EDL. This
164 paradigm simultaneously advances fundamental EDL mechanisms and enables programmable charge
165 manipulation for next-generation iontronic power, sensing, and neuromorphic devices.

166 **Results**

167 **Probing EDL Based on Triboelectric Charge Transfer**

168 In the CE process, the electron-cloud-potential-well model has been widely employed to describe charge
169 transfer driven by electron cloud interactions. Within this framework, atoms or molecules are depicted
170 as potential wells that spatially confine delocalized electron clouds. Each atom is modeled as a potential
171 well wherein valence electrons are weakly bound, collectively constituting the atomic or molecular
172 electron cloud. As shown in Fig. 1a, d denoted the distance between electron clouds. Before contact,
173 electrons were trapped within these wells, preventing inter-material transfer. Upon contact between water
174 molecules and a dielectric surface, screening-induced electron cloud overlap transforms the initially
175 symmetric potential wells into asymmetric double-well configurations. This asymmetry facilitates the
176 quantum tunneling of electrons from the water molecules to the solid surface, thereby initiating charge
177 transfer. As illustrated in Fig. 1b, thermal motion and interfacial pressure drive water molecules and
178 solvated ions, primarily H_2O , cations, and anions, into dynamic collisions with the solid interface. These
179 collisions induce electron transfer through electron cloud overlaps, alongside interfacial ionization
180 reactions. The dielectric solid undergoes electronic polarization and partial ionization of surface groups,
181 generating localized charges that form the IHP with specifically adsorbed ions. Liquid ions then
182 redistribute to form the OHP, together constituting the Stern layer where most of the interfacial potential
183 drop occurs. Beyond this, the diffuse layer extended into the bulk solution, completing the EDL structure.
184 The TENG-based triboelectric charge transfer detection setup comprises a PTFE film for CE and a copper
185 layer functioning as the induction electrode (Fig. 1c). When deionized (DI) water contacted the solid
186 surface, CE-induced electron transfer occurred with the self-ionization of water, generating ions that
187 participated in interfacial ion exchange. Following electron transfer, ions were adsorbed onto the surface,
188 further promoting interfacial ion accumulation. This combined transfer of electrons and ions imparted a
189 net negative charge to the solid surface, which subsequently attracted counterions from the liquid,
190 culminating in EDL formation at the solid-liquid interface.

191 Upon the introduction of an electrolyte, the EDL underwent further modulation through complex
192 interactions between the added cations and anions and the pre-existing interfacial environment. These
193 ions reshaped the interfacial charge distribution, electrostatic potential, and ionic composition, with

194 outcomes strongly governed by ion-specific parameters such as size, valency, and hydration
195 characteristics. Together, these factors defined the structural and dynamic properties of evolving EDL.
196 For symmetric electrolytes such as LiCl solution, charge transfer gradually decreased with increasing
197 concentration and plateaued upon reaching a critical concentration (Figs. 1d and S1). LiCl dissociated
198 into Li^+ and Cl^- in water, increasing the population of free ions available for EDL formation at the solid-
199 liquid interface. Rising ionic concentration promoted the development of a more compact EDL due to
200 the elevated ion density. Once a more compact EDL formed in LiCl, it effectively attenuated electron
201 transfer, reducing the charge output during CE^[13]. In contrast, asymmetric electrolytes introduced
202 additional complexity. Prior studies have reported charge inversion^[44, 45] in systems with ion size, valence,
203 or polarizability disparities, where disrupted ion-ion correlations within the EDL could lead to local
204 overcompensation of surface charge and even net charge reversal. However, the mechanisms by which
205 ionic asymmetric modulated EDL structure remain poorly understood. In this study, EDL behavior in
206 high-concentration asymmetric electrolytes was investigated to address this gap. Li[TFSI], characterized
207 by its combination of bulky anions and small cations, represented a prototypical asymmetric electrolyte
208 system to elucidate the impact of ionic asymmetric (Fig. S2a). To assess the impact of EDL formation
209 dynamics under such ionic asymmetry, Li[TFSI] was investigated using the same TENG-based
210 triboelectric charge measurements. At an initial concentration of 10^{-3} M, the transferred charge was
211 positive. As the concentration increased to 10^{-2} M, the charge transfer decreased but remained positive.
212 However, upon further increasing the concentration to 10^{-1} M, the transferred charge inverted, becoming
213 negative, a signature of altered EDL formation dynamics. This negative charge transfer persisted at 1 M,
214 indicating a concentration-dependent transition in interfacial charge behavior driven by the asymmetric
215 nature of the electrolyte (Figs. 1e, S3). [EMIM]Cl, an electrolyte featuring large-sized cations and smaller
216 anions (Fig. S2b), was selected to further examine EDL formation and dynamics in high-concentration
217 asymmetric systems. The transferred charge was also observed to be initially positive at low
218 concentrations. However, as the concentration increased, the charge transferred progressively declined
219 and ultimately inverted to negative, reflecting a distinct ion-specific EDL formation mechanism driven
220 by the asymmetric ion sizes (Figs. 1f, S4). It should also be noted that triboelectric charge measurements
221 utilizing TENG on solid LiCl, Li[TFSI], and [EMIM]Cl revealed charge polarities consistent with the

direction of charge transfer observed in their respective high-concentration solutions (Figs. S5, S6, and S7).

To verify the correlation between electrolyte-dependent electrical outputs and distinct EDL formation mechanisms in CE, the triboelectric charge transfer behaviors of LiCl, Li[TFSI], and [EMIM]Cl solutions were systematically characterized under varying experimental conditions (Fig. 1g). The PTFE film was installed at a 45° incline, and a grounded syringe was used to continuously release a droplet of approximately 25 μL of solution onto the film. When the droplet slid across the PTFE film into the Faraday cylinder, the triboelectric charge carried by the droplet was measured. When LiCl solution was used, the droplet-transferred charge progressively decreased with increasing concentration (Figs. 1h, S8), as the formation of a more compact EDL enhanced charge screening and suppressed electron transfer. In the case of Li[TFSI], a similar trend was observed at lower concentrations, with the transferred charge decreasing as the EDL became compact. When the concentration exceeded 10^{-1} M, changes in the formation mechanism of the EDL led to a reversal of the transferred charge from positive to negative (Figs. 1i, S9). A comparable inversion was also found in [EMIM]Cl solutions, where low-concentration measurements yielded positive charge transfer, followed by a polarity reversal at higher concentrations (Figs. 1j, S10). To further investigate interfacial charge behavior, each electrolyte solution was brought into contact with the PTFE surface and then dried, after which the surface potential of the PTFE was measured using KPFM. The resulting surface potential reflected the net transferred charge during the CE process (Fig. 1k). Initially, the surface potential of the PTFE film after CE with DI water was -1.80 V. When CE was conducted using LiCl solutions of increasing concentration, the surface potential rose from -1.64 V at 10^{-3} M to -0.53 V at 1 M while remaining consistently negative. This indicates that the liquid phase generated positive charges, and the PTFE film acquired negative charges throughout the process (Fig. 1l). When Li[TFSI] solutions of varying concentrations were used, the surface potential remained negative at 10^{-3} M and 10^{-2} M (~ -1 V to -0.6 V) but reversed to positive at 10^{-1} M and 1 M (~ 0.4 V to 0.2 V) (Fig. 1m), indicating that Li[TFSI] generated positive charges during CE at low concentrations, while producing negative charges at higher concentrations. A similar trend was observed for [EMIM]Cl solutions: the surface potential was negative at 10^{-3} M and 10^{-2} M (~ -0.6 V) but became positive as the concentration increased to 10^{-1} M and 1 M (~ 0.4 V to 0.2 V) (Fig. 1n). These

250 results, consistent across KPFM, TENG, and Faraday cylinder measurements, confirm asymmetric
251 electrolytes drive charge inversion in CE. By analyzing the triboelectric output signals, the dynamic
252 evolution of the EDL might be revealed. These TENG-based triboelectric charge transfer measurements
253 offer a powerful, multifunctional probe for in situ characterization of EDL formation and interfacial
254 charge behaviors at solid-liquid interfaces.

255 Charge inversion may stem from factors such as ionic asymmetry, hydrophobicity, and surface
256 charge density. Asymmetric ions intensify ion-ion correlations within the EDL, enabling charge
257 overcompensation. Hydrophobic ions tend to adsorb at interfaces, while high surface charge densities
258 enhance counterion accumulation. Although these phenomena are supported by both experiments and
259 simulations, their molecular origins remain poorly understood due to the complex interplay of ionic
260 interactions and interfacial dynamics. Importantly, the ability to harness charge inversion offers powerful
261 means for manipulating interfacial charge behavior in advanced iontronic systems. For instance, charge
262 reversal in polyelectrolyte-confined fluid memristors^[19, 44, 45] enables precise control of ionic dynamics,
263 effectively bridging chemical and electrical signals, a key mechanism underpinning the development of
264 bio-inspired neuromorphic computing architectures. In biological neural networks, chemical stimuli
265 often trigger electrical responses, with charge reversal serving as the fundamental physical basis for this
266 transduction. By regulating charge reversal behavior, the accumulation and dissipation of ions in
267 nanoscale channels can be effectively controlled, allowing for the emulation and control of synaptic-like
268 memory behaviors. Controlled ionic charge inversion in a polyelectrolyte-confined fluidic memristor
269 could enable bio-inspired neuromorphic computing, bridging chemical and electrical signaling for next-
270 generation adaptive neuroprosthetics and brain-machine interfaces.

271 **Investigating the Formation of EDL in Asymmetric Electrolytes**

272 To further investigate the mechanism behind charge inversion in asymmetric electrolytes during the CE
273 process and to elucidate the formation of the EDL, a combined approach involving experimental
274 measurements and MD simulations was employed. This integrated analysis aimed to enhance the
275 accuracy and reliability of triboelectric charge transfer probe for studying EDL formation in detail. The
276 conductivity of each solution at various concentrations was measured using a conductivity meter,
277 showing a gradual increase in conductivity with increasing concentration (Fig. S11a). The ion mobility

278 was calculated using the Nernst-Einstein equation^[46], and the relationship between ion mobility (u) and
 279 ionic conductivity (K) can be expressed by the following equation:

$$280 \quad u = \frac{K}{c \cdot |z| \cdot F} \quad (1)$$

281 where c is the ion concentration, z is the ion charge, and F is the Faraday constant. The ion mobility of
 282 LiCl and [EMIM]Cl gradually decreased with increasing concentration. However, in the case of Li[TFSI],
 283 the ion mobility initially increased as the concentration rose from 10^{-3} M to 10^{-2} M, but it began to
 284 decrease as the concentration continued to increase (Fig. S11b). The relationship between diffusion
 285 coefficient (D) and ion mobility (u) can be expressed by the following equation:

$$286 \quad D = u \cdot \frac{K_B \cdot N_A \cdot T}{|z| \cdot e \cdot N_A} = u \cdot \frac{R \cdot T}{|z| \cdot F} \quad (2)$$

287 where K_B is the Boltzmann constant, N_A is the Avogadro constant, T is the absolute temperature, e is the
 288 elementary charge, and R is the gas constant. The diffusion coefficient of LiCl and [EMIM]Cl decreased
 289 with an increase in concentration, while the diffusion coefficient of Li[TFSI] initially increased and then
 290 decreased, remaining consistently smaller than that of LiCl at the same concentration (Fig. S12). Since
 291 the ion conductivity meter provides only the overall diffusion coefficient of the electrolyte and cannot
 292 resolve the mobility of individual ionic species, MD simulations were employed to calculate the diffusion
 293 coefficients of individual ions in detail. The composition and configuration of the simulation boxes used
 294 for these calculations are summarized in Table S1. By adding different amounts of Li^+ and Cl^- in the
 295 same system to achieve the concentrations used in the experiments (Fig. S13). However, as the
 296 concentration continued to increase, the diffusion coefficients exhibited changes, with Cl^- consistently
 297 exhibiting a higher diffusion coefficient than Li^+ regardless of the concentration (Figs. 2a, S14 and
 298 Supplementary Data 1-4). During the CE process, electron transfer occurs first, followed by the
 299 adsorption of Cl^- onto the PTFE surface, which imparts a net negative charge to the PTFE and establishes
 300 the IHP of the EDL. Due to the high hydration-free energy of Li^+ , it typically could not escape from its
 301 hydration shell to enter the dipole layer of water molecules and thus could not directly enter the IHP. As
 302 a result, the hydrated Li^+ ions formed the OHP, completing the EDL structure (Figs. 2b,2c). This EDL
 303 formation inhibited electron transfer, thereby reducing the amount of transferred charge. As
 304 concentration increased, the higher ionic strength led to a denser EDL, suppressing electron transfer.
 305 However, in the case of LiCl, the overall charge remained negative across all concentrations. To replicate

306 the experimental conditions in simulations, varying amounts of Li^+ and $[\text{TFSI}]^-$ were introduced into the
307 same system to construct the corresponding electrolyte concentrations (Fig. S15). Notably, a distinct
308 deviation from the behavior observed in LiCl solutions was found: at lower concentrations (10^{-3} M to
309 10^{-2} M), the diffusion coefficient of $[\text{TFSI}]^-$ exceeded that of Li^+ , whereas at higher concentrations
310 (10^{-1} M and 1 M), $[\text{TFSI}]^-$ exhibited a lower diffusion coefficient than Li^+ , highlighting a concentration-
311 dependent reversal in ionic mobility likely driven by the increasing steric hindrance and aggregation
312 tendencies of bulky $[\text{TFSI}]^-$ (Figs. 2d, S16 and Supplementary Data 5-8). During the formation of the
313 EDL, anions are generally more prone to specific adsorption than cations. At concentrations between
314 10^{-3} M and 10^{-2} M, the migration speed of $[\text{TFSI}]^-$ was higher than that of Li^+ , resulting in an EDL
315 formation process like that observed with LiCl (Fig. 2e). However, when the concentration exceeded
316 10^{-1} M, $[\text{TFSI}]^-$ diffusion slowed significantly due to steric hindrance, while Li^+ remained highly mobile.
317 During the CE process, electron transfer rendered the PTFE surface negatively charged, triggering the
318 rapid migration of Li^+ toward the surface to form the OHP of the EDL. The bulky $[\text{TFSI}]^-$, unable to
319 enter the Stern layer due to size exclusion, was instead electrostatically adsorbed in the diffuse layer (Fig.
320 2f). This substantial accumulation of Li^+ near the surface led to charge overcompensation, ultimately
321 reversing the net surface charge from negative to positive.

322 Temperature critically modulates both CE charge transfer kinetics and ion diffusion behavior^[34]. To
323 explore these effects, MD simulations were conducted at different temperatures, focusing on a
324 concentration of 10^{-1} M where charge inversion was experimentally observed. In MD simulations, when
325 the electrolyte was 10^{-1} M LiCl , the diffusion coefficient of Cl^- consistently remained higher than that of
326 Li^+ across the temperature range of 273.15 K to 333.15 K, indicating that temperature-enhanced ionic
327 mobility without altering the relative diffusion hierarchy (Figs. 2g, S17 and Supplementary Data 9-12).
328 The migration speed of Cl^- consistently exceeded that of Li^+ across all temperatures, and the EDL
329 formation mechanism in 10^{-1} M LiCl remained unchanged. However, when the solution was switched to
330 10^{-1} M $\text{Li}[\text{TFSI}]$, a distinct temperature-dependent shift in ion mobility was observed. At 273.15 K and
331 293.15 K, the diffusion coefficient of $[\text{TFSI}]^-$ was lower than that of Li^+ , consistent with charge inversion
332 driven by the preferential accumulation of Li^+ at the interface. As the temperature increased to 313.15 K
333 and 333.15 K, the diffusion coefficient of $[\text{TFSI}]^-$ surpassed that of Li^+ , suggesting a reversal in dominant

334 ionic migration and a potential shift in EDL structure and interfacial charge behavior (Figs. 2h, S18 and
335 Supplementary Data 13-16). To verify the accuracy of the simulation and avoid discrepancies between
336 the real experiment and the simulation, further experiments were conducted to validate the simulation,
337 and triboelectric charge measurement facilities were performed using 10^{-1} M LiCl solutions at varying
338 temperatures. The results revealed a gradual decline in transferred charge with increasing temperature,
339 while the charge polarity remained positive. This suggests that elevated thermal energy weakens
340 interfacial charge transfer without reversing the EDL polarity in relatively symmetric electrolytes. This
341 effect may arise from the enhanced mobility of Li^+ and Cl^- ions at higher temperatures, which accelerates
342 EDL formation and increases charge screening at the interface (Fig. 2i). In the MD simulation, it was
343 found that Li[TFSI] exhibits a diffusion coefficient inversion phenomenon with temperature changes.
344 Therefore, the 10^{-1} M Li[TFSI] solution was selected for further investigation, which exhibited charge
345 reversal in previous experiments. When the experimental temperature was 273.15K and 293.15 K, the
346 transferred charge was negative, and a charge reversal occurred. However, when the temperature
347 increased to 313.15K and 333.15 K, the transferred charge reversed to being positive, with no charge
348 reversal observed (Fig. 2j). These findings further validated the proposed model of EDL formation in
349 asymmetric electrolytes and provided additional support for the reliability of using TENG-based
350 triboelectric charge transfer probe for detection across different temperatures.

351 Upon validation of the simulation accuracy, it was applied to the [EMIM]Cl solution (Fig. S19). For
352 [EMIM]Cl, the overall diffusion coefficient first increased and then decreased, while the diffusion
353 coefficient of Cl^- consistently exceeded that of the bulkier $[\text{EMIM}]^+$ at all concentrations. Crucially, this
354 pronounced mobility disparity proved decoupled from charge inversion phenomena, revealing that steric
355 constraints and solvation structure reorganization, rather than simple ion mobility gradients, govern EDL
356 restructuring. This mechanistic disconnect underscores incomplete understanding of asymmetric
357 electrolyte behavior at dielectric interfaces, necessitating further investigation (Figs. S20, S21 and
358 Supplementary Data 17-20). 3D-AFM enabled simultaneous scanning in the XY plane and along the Z
359 axis for each X coordinate, allowing the probe to map a volumetric region extending tens of nanometers
360 above the sample surface. By assembling a series of XZ cross-sectional images, a detailed reconstruction
361 of the solid-liquid interfacial architecture becomes possible. To further validate the proposed model for

EDL formation in asymmetric electrolytes, 3D-AFM was employed to perform high-resolution nanoscale imaging (Fig. 3a). When the tip approaches the solid-liquid interface, it encounters long-range repulsive or attractive forces from ion distributions in the EDL, resulting in subtle mechanical deflections of the cantilever. These are recorded as force-distance curves and analyzed to extract information about the layering structure. In the experimental setup, the electrolyte solution was confined between a SiO₂ substrate and a top glass surface, with the 3D-AFM cantilever immersed in the electrolyte (Fig. S23). Following CE between the solution and the SiO₂ surface, electron or ion transfer occurred, forming an EDL. This methodological optimization substitutes SiO₂ for characterization due to PTFE's inherent electrostatic interference, which precludes reliable characterization. Nevertheless, PTFE, selected for CE experiments given its superior dielectric constant and electronegativity, yielded consistent charge inversion signatures (Figs. 1 and S22). By scanning the SiO₂ interface, the adsorption profile was visualized, allowing estimation of the Stern layer thickness and direct assessment of the EDL formation model. In the case of LiCl, the thickness of the structured interfacial layer was found to decrease slightly with increasing concentration, although the overall change remained relatively small (Fig. S24). As the electrolyte concentration increased, the EDL became progressively denser, resulting in a slight reduction in the thickness of the Stern layer, consistent with experimental observations. For [EMIM]Cl solutions, a similar trend was observed: the thickness of the interfacial layered structure decreased gradually with increasing concentration, mirroring the behavior observed with LiCl (Fig. S25). To further validate these findings, AFM force-curve scanning was conducted in tapping mode on SiO₂ surfaces exposed to LiCl and [EMIM]Cl solutions of varying concentrations. For each condition, force curves were recorded at ten different points and averaged. The resulting phase and amplitude profiles (Figs. S26, S27) revealed two distinct hydration layers. Similar double-layered hydration structures were observed with LiCl and [EMIM]Cl (Figs. S28, S29). The force curves were converted into force-distance curves using the method of Allard J. Katan^[47], revealing oscillatory behavior alternating between attractive and compensatory regions, peaking upon tip–surface contact. To facilitate interpretation, the horizontal axis of the force-distance curves was shifted by subtracting the probe displacement at the point of surface contact, such that the zero point corresponds to the effective probe-surface distance. Notably, the peak-to-peak distance in the LiCl solution remained largely unchanged across different concentrations, consistent with

390 observations from 3D-AFM measurements (Fig. S30). These findings confirmed that the fundamental
391 structure of the EDL in LiCl solutions remained largely invariant across different concentrations, as
392 evidenced by the consistent peak-to-peak distances, in agreement with 3D-AFM measurements. A similar
393 trend was observed in [EMIM]Cl solutions, where the interpeak distance also exhibited minimal variation
394 with increasing concentration (Figs. 3b, S31). However, this similarity is not indicative of experimental
395 insensitivity or limitations but instead reflects a meaningful physical outcome. The AFM technique
396 primarily detects long-range electrostatic, and hydration forces normal to the interface, and is most
397 sensitive to macroscopic features such as the presence, thickness, and layering of the EDL. The consistent
398 force oscillation patterns and interpeak distances across concentrations indicate that the stratified
399 structure of the EDL, comprising the IHP, OHP, and diffuse layer, remains largely intact even at high
400 ionic strength. In other words, concentration variation does not lead to the collapse, merging, or
401 reconstruction of the overall double-layer architecture, but rather preserves its spatial profile. This
402 suggests that the charge reversal phenomenon in [EMIM]Cl did not fundamentally alter the basic
403 structure of the EDL, likely due to the consistent specific adsorption behavior of the same Cl^- anions at
404 the solid interface. The stability of the EDL may be attributed to the overcompensation of surface charge
405 by the adsorbed ions, which preserves the spatial integrity of the IHP and OHP despite variations in ion
406 composition and polarity.

407 To resolve molecular-scale mechanisms of EDL formation, SERS was employed. Direct
408 interrogation of PTFE-electrolyte interfaces remains precluded by the material's dielectric character and
409 absence of plasmonic activity. To overcome this constraint, we engineered an electrochemically
410 modulated SERS platform using Au nanoparticles (Au-NPs)-modified electrodes under precisely
411 controlled electric fields. This system simulates the interfacial electric field generated by CE without
412 replicating the exact PTFE interface, enabling quantitative analysis of CE-induced field magnitude and
413 orientation effects on EDL restructuring dynamics. Using ~ 60 nm Au-NPs modified Au electrode as the
414 plasmonic substrate (Fig. 3c). This approach enabled the identification of species-specific interactions
415 and the structural evolution of the interface under varying conditions. The Au-NPs create strong local
416 electromagnetic fields under laser excitation, enhancing Raman signals from adsorbed molecular species.
417 To emulate the electrostatic environment associated with EDL formation on the dielectrics under

418 triboelectric fields induced by CE, an external electric field was applied via a conventional
419 electrochemical setup, mimicking the interfacial potential generated by CE-driven charge separation. In
420 the experiment, the solution was placed on a flat Au substrate, and then Au-NPs were transferred onto
421 the Au surface, thereby constructing the Au-NPs/solution/Au electrode. Under appropriate laser
422 irradiation, the highly SERS-active Au-NPs generated an extremely strong electromagnetic field, which
423 enhanced the Raman signal of the adsorbed species. According to prior experimental and theoretical
424 studies, solid-liquid CE generates strong localized electric fields at the interface due to charge separation
425 and accumulation during contact or sliding. Reported field strengths can reach 10^8 - 10^9 V/m^[48-50],
426 confined within the EDL region, typically ~ 1 nm thick under high-concentration electrolytes. To estimate
427 the effective interfacial potential induced by CE, the classical relation is applied:

$$428 \quad E = \frac{V}{d} \quad (3)$$

429 where E is the electric field strength, V the electric potential, and d the EDL thickness (~ 1 nm).
430 Assuming a field strength of 10^9 V/m, the corresponding potential drops across the interface is
431 approximately 0.1-1 V. Thus, an applied bias of -1 V and -0.1 V in SERS experiments serves as a
432 reasonable approximation of the local electrostatic potential experienced by ions during CE, enabling
433 simulation of field-driven ion arrangements. When the asymmetric electrolyte [EMIM]Cl was used, its
434 Raman response exhibited distinct trends. As shown in Figs. 3d, S32, under an applied negative potential
435 (-1 V), the Raman signal remained largely unchanged between 10^{-3} M and 10^{-2} M. However, at 10^{-1} M,
436 a pronounced increase in the C-N stretching peak at 1565 cm^{-1} was observed, indicating enhanced
437 [EMIM]⁺ adsorption at the interface. Further increasing the concentration to 1 M produced only minor
438 additional changes, suggesting that the interfacial structure had reached saturation. When the applied
439 potential was adjusted to -0.1 V, the Raman signal remained consistent with that observed at -1 V, with
440 a distinct increase occurring at 10^{-1} M. This enrichment is attributed to the preferential adsorption and
441 field-driven organization of bulky [EMIM]⁺ cations in the OHP. Previous studies have suggested that ion
442 hydrophobicity^[19] can promote overcompensation, thereby inducing charge reversal. To examine this
443 effect, glass slides were treated with electrolyte solutions of varying concentrations, dried, and
444 subsequently assessed via contact angle measurements using deionized water. With increasing LiCl
445 concentration, the contact angle decreased, indicating enhanced surface hydrophilicity. In contrast,

446 higher concentrations of [EMIM]Cl led to increased contact angles, reflecting a shift toward greater
447 surface hydrophobicity (Fig. S34). Meanwhile, plasma treatment was applied to modify the PTFE surface
448 to enhance its hydrophilicity (Fig. S35). Subsequently, triboelectric charge transfer measurements were
449 conducted using [EMIM]Cl solutions of varying concentrations on both untreated (hydrophobic) and
450 plasma-treated (hydrophilic) PTFE surfaces under otherwise identical conditions. The results revealed a
451 clear distinction: on the untreated PTFE surface, as the [EMIM]Cl concentration increased beyond 10^{-1}
452 M, the transferred charge shifted from negative to positive. In contrast, for the plasma-treated, more
453 hydrophilic surface, although the total charge transfers slightly decreased with increasing electrolyte
454 concentration, no charge polarity reversal was observed across the entire tested concentration range (Fig.
455 S36). These results confirmed that charge reversal occurs when [EMIM]⁺ exhibits hydrophobic
456 characteristics. As shown in Fig. 3e, at lower concentrations, EDL formation was primarily driven by
457 electron transfer arising from molecular thermal motion at the solid-liquid interface, along with anion
458 adsorption from electrolyte dissociation. This process established the IHP, after which the negatively
459 charged surface attracted large [EMIM]⁺ cations as counterions to form the OHP, completing the EDL
460 structure. The IHP is predominantly populated by smaller Cl⁻ anions, while [EMIM]⁺ cations exist in
461 dilute form within the OHP, resulting in a net negative interfacial charge. In contrast, at higher
462 concentrations (Fig. 3f), [EMIM]⁺ cations accumulate extensively in the OHP due to enhanced ion-field
463 interactions and possibly hydrophobic self-association, leading to local charge overcompensation and
464 eventual polarity inversion. Li[TFSI] solutions at two representative concentrations (10^{-2} M and 10^{-1} M)
465 were analyzed using the same SERS substrate and experimental setup as for [EMIM]Cl. As shown in the
466 newly added Fig. S33, the Raman spectra exhibit two distinct peaks at approximately 253 cm^{-1} and
467 295 cm^{-1} , corresponding to the vibrational mode of Li⁺-OH⁻ complexes and the symmetric/asymmetric
468 stretching of the -CF₃ groups within the [TFSI]⁻ anion, respectively. Notably, both peaks show
469 significantly increased intensity at 10^{-1} M, indicating enhanced accumulation of Li⁺ and [TFSI]⁻ at the
470 interface with increasing concentration. These spectral changes are consistent with the formation of a
471 more compact and structured EDL under high ionic strength. In particular, the stronger Li⁺ signal
472 suggests that, due to its small ionic radius and high charge density, Li⁺ is preferentially attracted to the
473 negatively charged PTFE surface generated during CE, facilitating its enrichment at the OHP and

474 promoting the development of a dense EDL. These findings highlight the utility of TENG-based
475 triboelectric charge transfer as a precise and versatile probe for characterizing EDL formation and charge
476 evolution at solid-liquid interfaces.

477 **Formation Mechanisms and Evolution of EDL in Asymmetric Electrolyte Systems**

478 The formation and evolution of the EDL in asymmetric electrolytes were governed by a sophisticated
479 interplay of multiple physicochemical parameters, including ionic size asymmetry, hydrophobic effects,
480 concentration-dependent behaviors, and ion-ion correlation effects. These collective interactions induced
481 substantial deviations from classical EDL theories, particularly in high-concentration electrolyte systems
482 ($>10^{-1}$ M), where conventional mean-field approximations frequently failed to accurately capture the
483 observed interfacial phenomena. Through a combination of experimental observations and computational
484 analyses, distinct mechanisms responsible for EDL formation across various electrolyte systems were
485 identified, especially under high-concentration (exceeding 10^{-1} M) conditions. By integrating classical
486 EDL theory with triboelectric frameworks, we establish models resolving interfacial charge dynamics
487 across diverse solid-liquid interfaces, including high ionic strength regimes. It confirms material-agnostic
488 applicability. This model integrates the experimental observations into a form adapted for dielectric
489 interfaces, providing a coherent explanation of the charge inversion and structural transitions revealed in
490 the study. This paradigm simultaneously advances fundamental EDL mechanisms and enables
491 programmable charge manipulation for next-generation iontronic power, sensing, and neuromorphic
492 devices. When the solution used was a symmetric electrolyte, such as LiCl, it dissociated in water into
493 Li^+ and Cl^- ions, thereby increasing the number of available free ions in the system. As shown in Fig. 4a,
494 the ions in the LiCl solution (particularly Cl^- and Li^+) actively participated in the formation of the EDL
495 at the solid-liquid interface. Specifically, when the solution encountered the solid surface, Cl^- ions and
496 the electrons generated during the CE process jointly contributed to the formation of the IHP. Due to its
497 small size, high mobility, and specific adsorption capability, the Cl^- was able to rapidly adsorb onto the
498 solid surface, forming the foundation of the IHP together with the initially transferred electrons.
499 Meanwhile, due to the high hydration-free energy of Li^+ , it typically could not escape from its hydration
500 shell to enter the dipole layer of water molecules and thus could not directly enter the IHP. As a result,
501 the hydrated Li^+ ions formed the OHP. Together, these layers constituted the Stern layer which, along

502 with the diffuse layer, formed the complete EDL structure. As the concentration increased and exceeded
503 a critical threshold (10^{-1} M), the number of ions in the solution rose significantly, and the Coulombic
504 interactions between ions became substantially stronger, driving the formation of a more compact EDL,
505 as illustrated in Fig. 4b. When an asymmetric electrolyte solution with large-sized anions, such as
506 Li[TFSI] was used, the electrolyte dissociated in the solution, releasing small-sized Li^+ and large-sized
507 $[\text{TFSI}]^-$. Under low-concentration conditions ($<10^{-1}$ M), when the solution encountered a solid surface,
508 the IHP was rapidly formed^[2] (Fig. 4c). Meanwhile, Li^+ as counterions migrated to the solid surface
509 under the action of electrostatic attraction, forming the OHP and thereby completing the formation of the
510 EDL. However, when the solution concentration increased above 10^{-1} M, the diffusion speed of $[\text{TFSI}]^-$
511 significantly decreased and became lower than that of Li^+ . Under these conditions, the electrons initially
512 transferred during the CE process, together with the specifically adsorbed ions, rapidly formed the IHP.
513 Then, many Li^+ ions were quickly adsorbed onto the negatively charged solid surface, forming a dense
514 OHP, which might prevent the more slowly diffusing $[\text{TFSI}]^-$ anions from entering the Stern layer,
515 ultimately completing the construction of the EDL (Fig. 4d). When an asymmetric electrolyte solution
516 with large-sized cations, such as $[\text{EMIM}]\text{Cl}$, was used, the solution dissociated into large-sized $[\text{EMIM}]^+$
517 and small-sized Cl^- . Under low-concentration conditions ($<10^{-1}$ M), when the solution encountered a
518 solid surface, the electrons initially transferred during the CE process, together with Cl^- , rapidly formed
519 the IHP (Fig. 4e). Meanwhile, $[\text{EMIM}]^+$ as counterions, migrated to the solid surface under the action of
520 electrostatic attraction, forming the OHP and thereby completing the initial construction of the EDL.
521 However, when the solution concentration increased above 10^{-1} M, the IHP was still composed of
522 electrons and Cl^- . Due to changes in molecular conformation, enhanced interfacial interactions, and the
523 hydrophobic nature of $[\text{EMIM}]^+$, $[\text{EMIM}]^+$ exhibited a stronger tendency to adsorb onto the solid surface,
524 leading to over-absorption during the formation of the OHP, the positive charge density of the OHP
525 significantly increased, forming a diffuse layer with a net negative charge (Fig. 4f). Through TENG-
526 based triboelectric charge transfer measurements, a multifunctional and straightforward EDL
527 characterization method has been developed that surpasses traditional approaches. Corresponding EDL
528 theoretical models were proposed by combining classical models with the characteristics of different
529 electrolytes, enabling the elucidation of interfacial charge distribution and the mechanisms underlying

530 EDL formation. This work advances the fundamental understanding of charge regulation at dielectric
531 interfaces and paves the way for the application of iontronics in energy storage and intelligent sensing
532 technologies.
533

ARTICLE IN PRESS

534 Discussion

535 In this study, a triboelectric charge transfer approach utilizing a TENG is presented as a straightforward
536 probe for operando monitoring of the EDL at solid-liquid interfaces of non-conductive materials across
537 diverse electrolytes. A fundamental experimental gap was resolved by introducing the cost-effective and
538 operando methodology to probe EDLs at dielectric interfaces. Conventional techniques (e.g., KPFM,
539 electrochemical impedance) are fundamentally constrained at dielectric interfaces by conductivity
540 requirements, charge-trapping artifacts, and field-perturbation effects on EDL structures. Our
541 triboelectric charge transfer probe leverages CE as an intrinsic charge-transfer metric, enabling zero-bias,
542 electrode-free interrogation of EDL, unlocking previously inaccessible dielectric interfaces. In addition,
543 it confirms material-agnostic applicability to resolve interfacial charge dynamics across diverse solid-
544 liquid interfaces, including high ionic strength regimes. This paradigm simultaneously advances
545 fundamental EDL mechanisms and enables programmable charge manipulation for next-generation
546 iontronic power, sensing, and neuromorphic devices. By reconciling previously conflicting models
547 through a unified structural framework of EDL reorganization, these findings redefine the EDL as a
548 tunable functional platform for iontronic device engineering.

549

550 Methods**551 Materials**

552 The 50 μm -thick Polytetrafluoroethylene (PTFE) film (industrial grade) was purchased from Aladdin,
553 while the 5 mm-thick Polymethyl methacrylate (PMMA) film (industrial grade) was acquired from
554 Alibaba. The DI water with a resistivity of $18.2 \text{ M}\Omega\cdot\text{cm}$ used here was produced by a deionizer (HHitech,
555 China). Lithium chloride (LiCl) ($\geq 99\%$) was purchased from Aladdin, Lithium
556 bis(trifluoromethanesulphonyl)imide ($\text{Li}[\text{TFSI}]$) ($\geq 99\%$) was purchased from Aladdin, and 1-Ethyl-3-
557 methylimidazolium Chloride($[\text{EMIM}]\text{Cl}$) (98%) was purchased from Aladdin litmus reagent ($1\% \pm$
558 0.05%). Furthermore, all the chemical reagents used in this experiment are of analytical grade and require
559 no further treatment.

560 Characterization and Measurement

561 TENG-based triboelectric charge measurement experiment: The electrical output performance of the
562 triboelectric charge, including transferred charge, was tested using a programmable electrometer
563 (Keithley 6514). Real-time data collection was achieved through a software platform built based on
564 LabVIEW. The vertical uniaxial motor (Linmot HC14-10) was used to apply a variable vertical force.
565 The Faraday cylinder was used to test the charge carried by the droplets sliding through the tested film.
566 KPFM Experiments: The experiment was conducted using a commercial AFM device, Multimode 8
567 (Bruker, USA). A conductive tip (Oxford AC240TM-R3) was used as the probe.

568 3D-AFM Experiment: Scanning was performed in liquid using a Cypher ES system with environmental
569 control (Asylum Research, Oxford Instruments). The cantilever oscillation was driven by the BlueDrive
570 module. The probe (Arrow UHF Ultra High Frequency–Reflex coating) had a resonance frequency of
571 approximately 700-2000 kHz. Morphological images were collected at a scan rate of 10~15 Hz with a
572 resolution of 256×256 lines. For XZ images, the total X displacement consisted of 256 data points.

573 Raman spectra: Raman spectra ($100\text{-}4000 \text{ cm}^{-1}$) were acquired using a Horiba XploRA confocal Raman
574 microscope equipped with a 638 nm laser at 1% power for 30 s. A $50\times$ objective lens with a numerical
575 aperture (NA) of 0.5 was used for signal collection.

576

577

578 Simulations methods

579 MD simulations were performed using the LAMMPS package (29 Aug 2024 version). The general
580 Amber force field (GAFF) was applied to describe the [TFSI]⁻ anion, while the parameters for Li⁺ were
581 obtained from the optimized potentials for liquid simulations (OPLS) field. Water molecules were
582 modeled using the SPC/fw water model, and the [EMIM]⁺ cation was represented using the all-atom
583 optimized potentials for liquid simulations (OPLS-AA) field (Tables S2, S3 and S4). Long-range
584 electrostatic interactions were calculated using the particle-particle particle-mesh (PPPM) method, with
585 a cutoff distance of 12 Å applied for non-bonded interactions. A partial charge scaling approach is
586 employed, with the charge reduced from $\pm 1e$ to $\pm 0.8e$, to indirectly account for polarization effects,
587 thereby enhancing the consistency between structural and diffusion simulations.

588 Each simulation box was equilibrated for 2 ns in the isothermal-isobaric (NPT) ensemble to
589 determine the density, followed by an 8 ns production run in the canonical ensemble (NVT). The pressure
590 was maintained at 1 atm during all constant pressure simulations, facilitating isotropic volume
591 fluctuations. To ensure stability in bond lengths and angles of the water molecules, the SHAKE algorithm
592 was applied. Temperature control was achieved using a Nose-Hoover thermostat set to 293 K, with a
593 time step of 1 fs.

594

595 Data Availability

596 The authors declare that all the data that support the findings of this study are available within the article
597 and its supplementary information files. Source data is provided in this paper.

598

599 **References**

- 600 1. Greco, A. et al. Ultrafast aqueous electric double layer dynamics. *Science* **388**, 405-410 (2025).
- 601 2. Zhou, Y. et al. Real-time mass spectrometric characterization of the solid–electrolyte interphase of a
602 lithium-ion battery. *Nat. Nanotechnol.* **15**, 224-230 (2020).
- 603 3. Yang, L. et al. A moisture-enabled fully printable power source inspired by electric eels. *Proc. Natl.*
604 *Acad. Sci. U.S.A.* **118**, e2023164118 (2021).
- 605 4. Liu, J. et al. Nonaqueous Contact-Electro-Chemistry via Triboelectric Charge. *J. Am. Chem. Soc.*
606 **146**, 31574-31584 (2024).
- 607 5. Lin, S., Chen, X. & Wang, Z. L. Contact Electrification at the Liquid–Solid Interface. *Chem. Rev.*
608 **122**, 5209-5232 (2022).
- 609 6. Wu, Q., McDowell, M. T. & Qi, Y. Effect of the Electric Double Layer (EDL) in Multicomponent
610 Electrolyte Reduction and Solid Electrolyte Interphase (SEI) Formation in Lithium Batteries. *J. Am.*
611 *Chem. Soc.* **145**, 2473-2484 (2023).
- 612 7. Yuan, X. et al. Engineering battery corrosion films by tuning electrical double layer composition.
613 *Joule* **8**, 3038-3053 (2024).
- 614 8. Du, Y. et al. Multi-receptor skin with highly sensitive tele-perception somatosensory. *Sci. Adv.* **10**,
615 eadp8681 (2024).
- 616 9. Helmholtz, H. Ueber einige Gesetze der Vertheilung elektrischer Ströme in körperlichen Leitern mit
617 Anwendung auf die thierisch-elektrischen Versuche. *Annalen der Physik* **165**, 211-233 (1853).
- 618 10. Chapman, D. L. LI. A contribution to the theory of electrocapillarity. *The London, Edinburgh, and*
619 *Dublin Philosophical Magazine and Journal of Science* **25**, 475-481 (1913).
- 620 11. Grahame, D. C. The Electrical Double Layer and the Theory of Electrocapillarity. *Chem. Rev.* **41**,
621 441-501 (1947).
- 622 12. Lin, S., Xu, L., Chi Wang, A. & Wang, Z. L. Quantifying electron-transfer in liquid-solid contact
623 electrification and the formation of electric double-layer. *Nat. Commun.* **11**, 399 (2020).
- 624 13. Nie, J. et al. Probing Contact-Electrification-Induced Electron and Ion Transfers at a Liquid–Solid
625 Interface. *Adv. Mater.* **32**, 1905696 (2020).
- 626 14. Fedorov, M. V. & Kornyshev, A. A. Ionic Liquids at Electrified Interfaces. *Chem. Rev.* **114**, 2978-
627 3036 (2014).
- 628 15. Merlet, C. et al. Highly confined ions store charge more efficiently in supercapacitors. *Nat. Commun.*
629 **4**, 2701 (2013).
- 630 16. Esfandiari, A. et al. Size effect in ion transport through angstrom-scale slits. *Science* **358**, 511-513
631 (2017).
- 632 17. Calero, C., Faraudo, J. & Bastos-González, D. Interaction of Monovalent Ions with Hydrophobic
633 and Hydrophilic Colloids: Charge Inversion and Ionic Specificity. *J. Am. Chem. Soc.* **133**, 15025-15035
634 (2011).
- 635 18. Martín-Molina, A., Rodríguez-Beas, C. & Faraudo, J. Charge Reversal in Anionic Liposomes:
636 Experimental Demonstration and Molecular Origin. *Phys. Rev. Lett.* **104**, 168103 (2010).
- 637 19. He, X. et al. Chaotropic Monovalent Anion-Induced Rectification Inversion at Nanopipettes
638 Modified by Polyimidazolium Brushes. *Angew. Chem. Int. Ed. Engl.* **57**, 4590-4593 (2018).
- 639 20. Andersson, L., Sprik, M., Hutter, J. & Zhang, C. Electronic Response and Charge Inversion at
640 Polarized Gold Electrode. *Angew. Chem. Int. Ed.* **64**, e202413614 (2025).

- 641 21. Lin, K. et al. Charge Inversion and Calcium Gating in Mixtures of Ions in Nanopores. *J. Am. Chem.*
642 *Soc.* **142**, 2925-2934 (2020).
- 643 22. Parsons, R. The electrical double layer: recent experimental and theoretical developments. *Chem.*
644 *Rev.* **90**, 813-826 (1990).
- 645 23. Grahame, D. C. & Parsons, R. Components of Charge and Potential in the Inner Region of the
646 Electrical Double Layer: Aqueous Potassium Chloride Solutions in Contact with Mercury at 25°. *J. Am.*
647 *Chem. Soc.* **83**, 1291-1296 (1961).
- 648 24. Li, C.-Y. et al. In situ probing electrified interfacial water structures at atomically flat surfaces. *Nat.*
649 *Mater.* **18**, 697-701 (2019).
- 650 25. Gu, Y. et al. Resolving nanostructure and chemistry of solid-electrolyte interphase on lithium anodes
651 by depth-sensitive plasmon-enhanced Raman spectroscopy. *Nat. Commun.* **14**, 3536 (2023).
- 652 26. Yin, X.-T. et al. Unraveling the energy storage mechanism in graphene-based nonaqueous
653 electrochemical capacitors by gap-enhanced Raman spectroscopy. *Nat. Commun.* **15**, 5624 (2024).
- 654 27. Gonella, G. et al. Water at charged interfaces. *Nature Reviews Chemistry* **5**, 466-485 (2021).
- 655 28. Zhong, Y.-X. et al. Resolving Fine Structures of the Electric Double Layer of Electrochemical
656 Interfaces in Ionic Liquids with an AFM Tip Modification Strategy. *J. Am. Chem. Soc.* **136**, 14682-14685
657 (2014).
- 658 29. Tsai, W.-Y., Taberna, P.-L. & Simon, P. Electrochemical Quartz Crystal Microbalance (EQCM) Study
659 of Ion Dynamics in Nanoporous Carbons. *J. Am. Chem. Soc.* **136**, 8722-8728 (2014).
- 660 30. Bedzyk, M. J., Bommarito, G. M., Caffrey, M. & Penner, T. L. Diffuse-Double Layer at a Membrane-
661 Aqueous Interface Measured with X-Ray Standing Waves. *Science* **248**, 52-56 (1990).
- 662 31. Terris, B. D., Stern, J. E., Rugar, D. & Mamin, H. J. Contact electrification using force microscopy.
663 *Phys. Rev. Lett.* **63**, 2669-2672 (1989).
- 664 32. Sobarzo, J. C. et al. Spontaneous ordering of identical materials into a triboelectric series. *Nature*
665 **638**, 664-669 (2025).
- 666 33. Shi, L. et al. Water structure and electric fields at the interface of oil droplets. *Nature* **640**, 87-93
667 (2025).
- 668 34. Wei, Y. et al. Contact electrification at the solid-liquid transition interface. *Mater. Today* **74**, 2-11
669 (2024).
- 670 35. Li, X. et al. Harnessing triboiontronic Maxwell's demon by triboelectric-induced polarization for
671 efficient energy-information flow. *Joule* **9**, 101888 (2025).
- 672 36. Zhang, J., Lin, S., Zheng, M. & Wang, Z. L. Triboelectric Nanogenerator as a Probe for Measuring
673 the Charge Transfer between Liquid and Solid Surfaces. *ACS Nano* **15**, 14830-14837 (2021).
- 674 37. Zhang, J. et al. Triboelectric nanogenerators as a probe for studying charge transfer at liquid-solid
675 interface. *MRS Bull.* **50**, 327-335 (2025).
- 676 38. Zhang, J., Lin, S. & Wang, Z. L. Triboelectric Nanogenerator Array as a Probe for In Situ Dynamic
677 Mapping of Interface Charge Transfer at a Liquid-Solid Contacting. *ACS Nano* **17**, 1646-1652 (2023).
- 678 39. Zhang, J. et al. Triboelectric Spectroscopy for In Situ Chemical Analysis of Liquids. *J. Am. Chem.*
679 *Soc.* **146**, 6125-6133 (2024).
- 680 40. Li, R. et al. Probing Leidenfrost effect via contact electrification. *Nano Energy* **134**, 110570 (2025).
- 681 41. Li, X., Wang, Z. L. & Wei, D. Scavenging Energy and Information through Dynamically Regulating
682 the Electrical Double Layer. *Adv. Funct. Mater.* (2024).
- 683 42. Li, X. et al. Triboiontronics for efficient energy and information flow. *Matter* **6**, 3912-3926 (2023).

- 684 43. Li, X. et al. Triboiontronics with temporal control of electrical double layer formation. *Nat. Commun.*
685 **15**, 6182 (2024).
- 686 44. Xiong, T. et al. Neuromorphic functions with a polyelectrolyte-confined fluidic memristor. *Science*
687 **379**, 156-161 (2023).
- 688 45. He, X. et al. Micrometer-Scale Ion Current Rectification at Polyelectrolyte Brush-Modified
689 Micropipets. *J. Am. Chem. Soc.* **139**, 1396-1399 (2017).
- 690 46. France-Lanord, A. & Grossman, J. C. Correlations from Ion Pairing and the Nernst-Einstein
691 Equation. *Phys. Rev. Lett.* **122**, 136001 (2019).
- 692 47. Li, H. et al. Evolution of Interfacial Hydration Structure Induced by Ion Condensation and
693 Correlation Effects. *Angew. Chem. Int. Ed.* **64**, e202418029 (2025).
- 694 48. Kathmann, S. M., Kuo, I. F. W. & Mundy, C. J. Electronic Effects on the Surface Potential at the
695 Vapor–Liquid Interface of Water. *J. Am. Chem. Soc.* **130**, 16556-16561 (2008).
- 696 49. Hao, H., Leven, I. & Head-Gordon, T. Can electric fields drive chemistry for an aqueous
697 microdroplet? *Nat. Commun.* **13**, 280 (2022).
- 698 50. Xiong, H., Lee, J. K., Zare, R. N. & Min, W. Strong Electric Field Observed at the Interface of
699 Aqueous Microdroplets. *The journal of physical chemistry letters* **11**, 7423-7428 (2020).

700

701

Acknowledgments

This work is supported by the National Natural Science Foundation of China (Grant No. 22479016 D.W.).

Author Contributions Statement

D.W. and Z.L.W. proposed the idea and the project. D.W. designed all the experiments and supervised the whole project. Y.W., X.L., Y.G., and L.D. carried out the experiments in this paper and analyzed the corresponding data. Y.W., and X.L. analyzed the operation principle of TENG. X.G. and Z.Q.Z. performed molecular dynamics simulations and conducted the analysis. C.K., J.B., and A.I. performed and analyzed the Raman experiments. Y.G., L.D., and Z.Q.T. performed and analyzed the SERS experiments. All the authors discussed the results and commented on the manuscript. D.W. and W.Y. wrote this paper.

Competing Interests Statement

The authors declare no competing interests.

Figure Legends

Fig. 1 The mechanism of electrical double layer (EDL) formation induced by contact electrification (CE) and transferred charge at the solid–liquid (S-L) Interface of different electrolytes. a Schematic illustration of the electron-cloud-potential-well model. **b** Two-step model of EDL formation induced by CE. (Inner Helmholtz Plane (IHP), Outer Helmholtz Plane (OHP)) **c** Schematic of the triboelectric nanogenerator (TENG) for triboelectric charge transfer measurement facilities. **d** The transferred charge during CE between different concentrations of LiCl solution and PTFE. **e** The transferred charge during CE between different concentrations of Li[TFSI] solution and PTFE. **f** The transferred charge during CE between different concentrations of [EMIM]Cl solution and PTFE. **g** Schematic of the Faraday cylinder testing apparatus. **h** The transferred charge by droplets of LiCl solution passing over the PTFE film at different concentrations. **i** The transferred charge by droplets of Li[TFSI] solution passing over the PTFE film at different concentrations. **j** The transferred charge by droplets of [EMIM]Cl solution passing over the PTFE film at different concentrations. **k** Schematic of the kelvin probe force microscopy (KPFM) setup for measuring surface potential. **l** Surface potential of PTFE during CE with LiCl solution at different concentrations. **m** Surface potential of PTFE during CE with Li[TFSI] solution at different concentrations. **n** Surface potential of PTFE during CE with [EMIM]Cl solution at different concentrations.

731

732 **Fig. 2 Molecular dynamics (MD) simulations of LiCl and Li[TFSI] at different concentrations and temperatures, along**
733 **with tests at various temperatures. a** Diffusion coefficient of Li^+ and Cl^- at various concentrations. **b** Electrical double layer
734 (EDL) model of LiCl solution at a lower concentration. (inner Helmholtz plane (IHP), outer Helmholtz plane (OHP)) **c** EDL
735 model of LiCl solution at higher concentration. **d** Diffusion coefficients of Li^+ and $[\text{TFSI}]^-$ at various concentrations. **e** EDL
736 model of Li[TFSI] solution at a lower concentration. **f** EDL model of Li[TFSI] solution at higher concentration. **g** Diffusion
737 coefficients of Li^+ and Cl^- at different temperatures. **h** Diffusion coefficients of Li^+ and $[\text{TFSI}]^-$ at different temperatures. **i**
738 The charge transfer amount during contact electrification (CE) between a 10^{-1} M LiCl solution and PTFE at different
739 temperatures. **j** The charge transfer amount during CE between a 10^{-1} M Li[TFSI] solution and PTFE at different temperatures.

740

741 **Fig. 3 Investigation of electrical double layer (EDL) formation in asymmetric electrolytes using 3D-atomic force**
742 **microscopy (AFM) and surface-enhanced Raman spectroscopy (SERS). a** 3D-AFM schematic illustration. **b** Typical
743 hydration force-distance curve in solutions with different concentrations. **c** SERS schematic illustration. **d** Raman signals of
744 [EMIM]Cl solution at different concentrations and potentials. **e** EDL model of [EMIM]Cl solution at a lower concentration.
745 **f** EDL model of [EMIM]Cl solution at higher concentration.

746

747 **Fig. 4 Electrical double layer (EDL) models for different electrolytes. a** EDL model formed at lower concentrations in a
748 symmetric electrolyte solution. (inner Helmholtz plane (IHP), outer Helmholtz plane (OHP)) **b** EDL model formed at higher
749 concentrations in a symmetric electrolyte solution. **c** EDL model formed at lower concentrations in a larger anion electrolyte
750 solution. **d** EDL model formed at higher concentrations in a larger anion electrolyte solution. **e** EDL model formed at lower
751 concentrations in a larger cation electrolyte solution. **f** EDL model formed at higher concentrations in a larger cation electrolyte
752 solution.

753

754 **Editorial Summary**

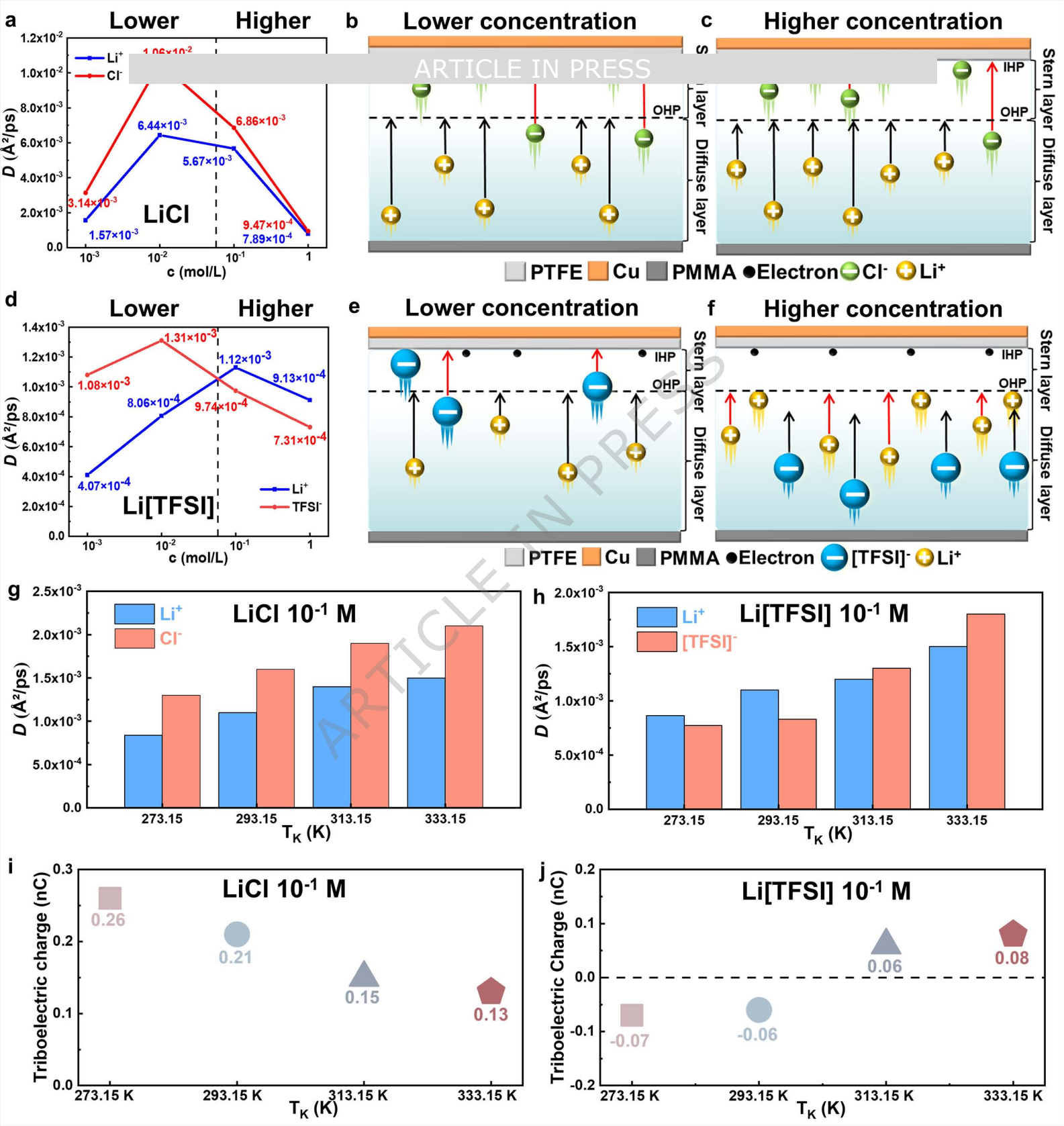
755 A triboelectric nanogenerator-based probe monitors the formation and evolution of the electrical double
756 layer at nonconductive interfaces via solid-liquid contact electrification.

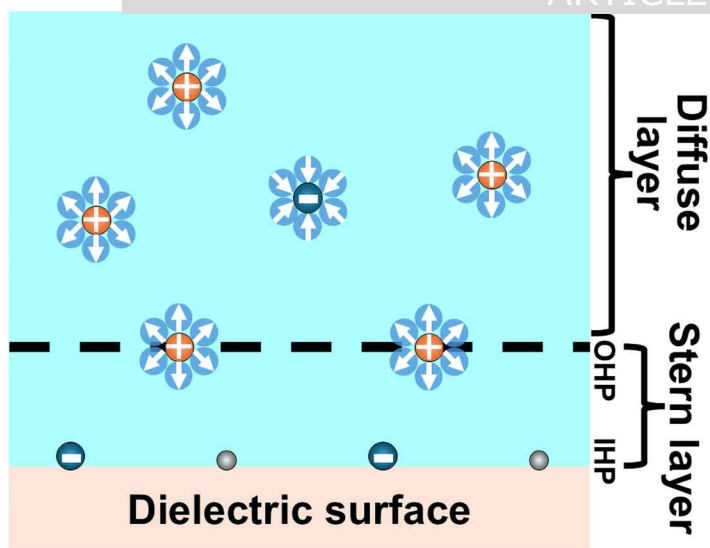
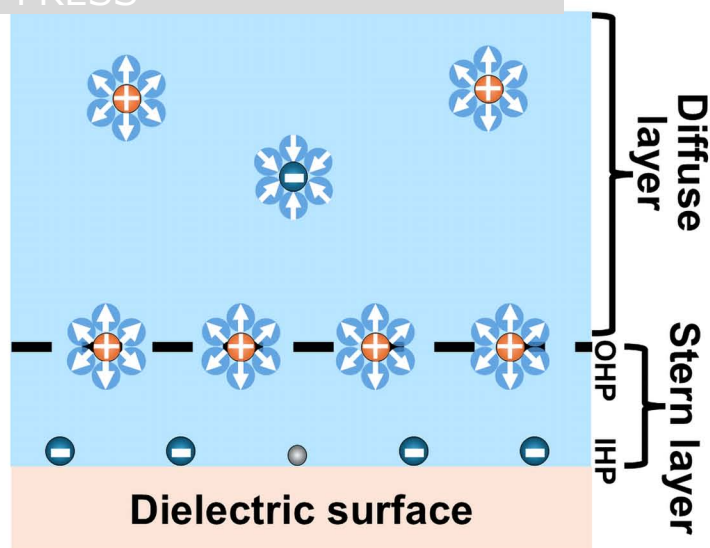
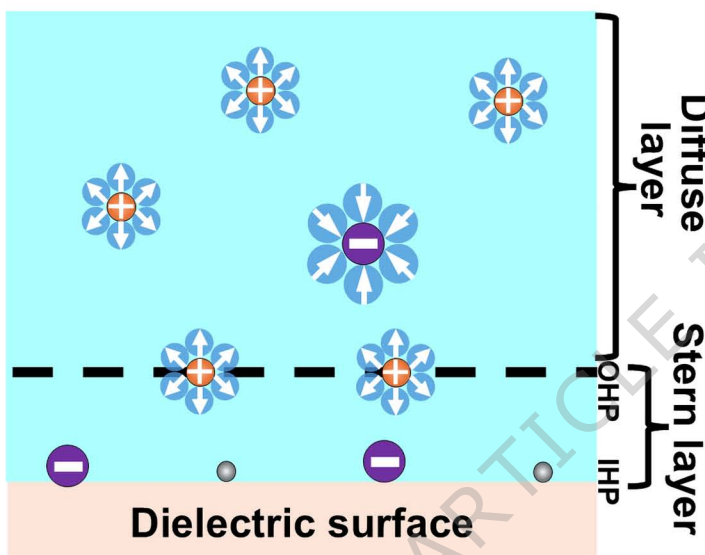
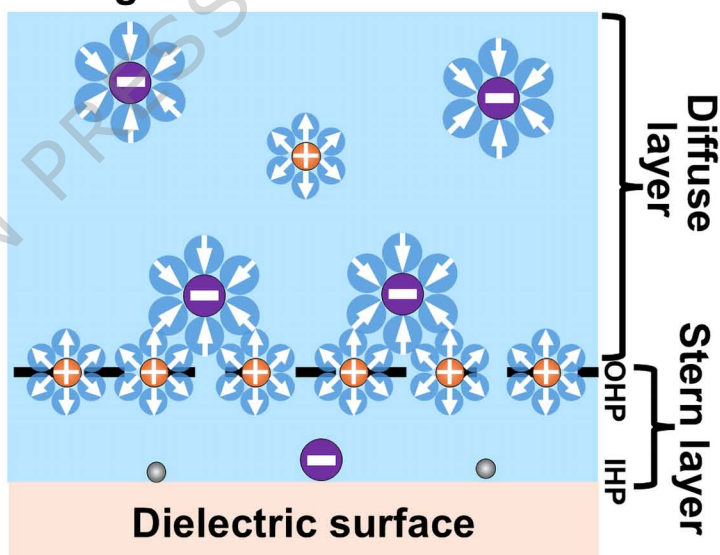
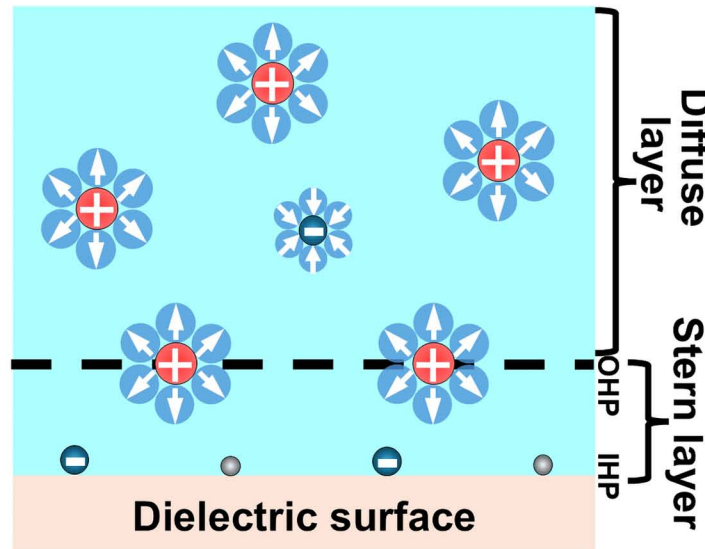
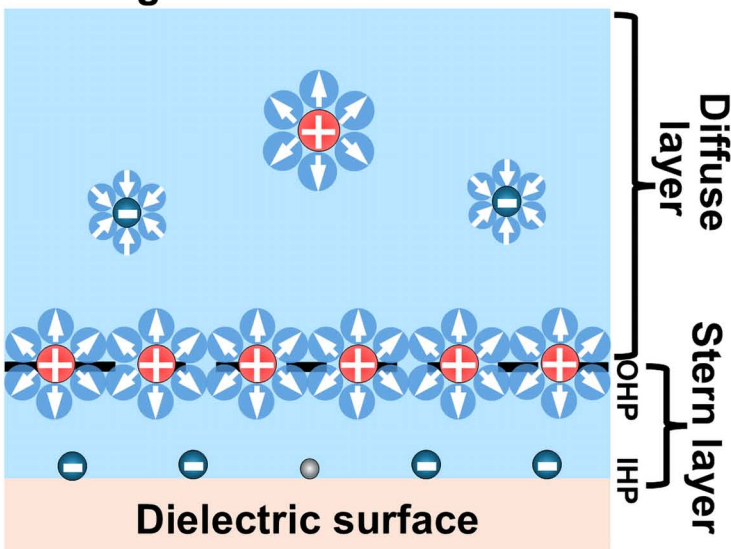
757

758 **Peer review information:** *Nature Communications* thanks Chang Hyuck Choi, Bin Kang and the other,

759 anonymous, reviewer(s) for their contribution to the peer review of this work. A peer review file is
760 available.
761

ARTICLE IN PRESS



a Symmetric electrolyte**b** Symmetric electrolyte**c** Larger anion electrolyte
Lower concentration**d** Larger anion electrolyte
Higher concentration**e** Larger cation electrolyte
Lower concentration**f** Larger cation electrolyte
Higher concentrations

● Electron ⊕ Cation ⊖ Anion ⊕ Larger cation
 ⊖ Larger anion ↻ Water molecule